Optics and Lasers in Engineering 152 (2022) 106949

Contents lists available at ScienceDirect

Optics and Lasers in Engineering

journal homepage: www.elsevier.com/locate/optlaseng

Surface topography measurement of microstructures near the lateral resolution limit via coherence scanning interferometry

Yifeng Sun[a], Zhishan Gao[a], Jianqiu Ma[a], Juntao Zhou[a], Pengfei Xie[a], Lingjie Wang[b,*], Lihua Lei[c], Yunxia Fu[c], Zhenyan Guo[a], Qun Yuan[a,*]

[a] School of Electronic and Optical Engineering, Nanjing University of Science and Technology, Nanjing 210094, China
[b] Key Laboratory of Optical System Advanced Manufacturing Technology, Changchun Institute of Optics, Fine Mechanics and Physics, Chinese Academy of Sciences, Changchun 130033, China
[c] Shanghai Key Laboratory of Online Test and Control Technology, Shanghai 201203, China

ARTICLE INFO

Keywords:
Surface topography
Microstructure
Coherence scanning interferometry
Lateral resolution limit

ABSTRACT

As a non-destructive method, coherence scanning interferometry is widely utilized for surface topography measurement of step microstructures in optical and integrated circuit fields. The measurements are always implemented near the lateral resolution limit of the system because the critical dimension of these microstructures is at the micron or sub-micron scale. However, in this case, not only is the image of microstructures blurred, but also the diffraction effects distort the measured topography near the step edges. The magnitude of distortion at a certain position appears to be related to its distance from the edges and the duty cycle of the microstructures. Therefore, it is necessary, although difficult, to improve the accuracy of topography measurement for microstructures if their images are blurred owing to the lateral resolution limit. When located far away from the step edges of microstructures, the coherence signals are normal and contain a single envelope with its peak corresponding to the surface height. However, the anomalous coherence signals containing two envelopes appear near the step edges. The peaks of these envelopes correspond to the top and bottom surfaces of step structures, thus distorting the coherence peak detection for topography measurement. Therefore, the primary issue is the determination of the correct envelope in the anomalous coherence signals that is achieved by distinguishing the current surface of step structures for each position. In this paper, we propose a binarization method based on edge localization to achieve surface distinguishment through the analysis of the contrast and intensity of the coherence signals. After determining the correct envelope, we construct a new form of wavelet family and employ the Morlet wavelet transform to calculate a split point for dividing the anomalous coherence signals. Finally, the effective coherence signals corresponding to the correct envelope are extracted. Surface topography measurement of the nanopillars on the metasurface is obtained from the extracted signals. These nanopillars are distributed with a varying duty cycle and their diameters range from 590 to 1350 nm, near the lateral resolution limit of 501.9 nm of the system. The topography of nanopillars is recovered from the field of view, while the diameter and height of different types of nanopillars are measured. The mean value and standard deviation of these two parameters are consistent with the results obtained via scanning electron microscopy.

Abbreviations

CSI	coherence scanning interferometry
CEEMDAN	complete ensemble empirical mode decomposition with adaptive noise
EMD	empirical mode decomposition
SEM	scanning electron microscopy
ALEP	amplitude of the left envelop peak
AREP	amplitude of the right envelop peak
IMF	intrinsic mode function
RCWA	rigorous coupled-wave analysis

1. Introduction

In recent years, there is a general trend of minimizing the component dimensions in the field of aerospace, integrated circuits and optical manipulation [1]. Thereby, surface topography measurement with high resolution has a profound effect on product quality control and manufacture monitoring. Coherence scanning interferometry (CSI) is widely applied for recovering the topography of microstructures. The lateral resolution depends on the imaging system of the interferometer. The height measurement is achieved by coherence peak detection of the coherence

* Corresponding authors.
E-mail addresses: wanglingjie@126.com (L. Wang), karmen86913@gmail.com (Q. Yuan).

https://doi.org/10.1016/j.optlaseng.2022.106949
Received 20 September 2021; Received in revised form 16 December 2021; Accepted 6 January 2022
Available online 12 January 2022

signals extracted from the scanning interferograms. Based on the linear theory [2], many studies concentrate on the three-dimensional transfer function of CSI and analyse the measurement errors induced by system aberrations or the tilt of the sample [3–5]. However, recovering the surface topography of microstructures, with dimensions near the lateral resolution limit of the system, is difficult based on linear theory. In this case, diffraction and scattering effects play an important role in the formation of interferograms [6–10]. Particularly, the complex diffraction effects have an obvious impact on the coherence signals generated for high-aspect-ratio structures [11]. In our previous study [12], we found the measured topography is distorted near the step edges of the nanopillars on the metasurface, when their critical dimension approaches the lateral resolution limit of CSI. Thus, we extracted the cross-sectional CSI images of the surface acquired at different axial locations for the analysis of the fringes generated near the edges. In this case, the additional fringes extend slightly in the air along the step edges and induce anomalous coherence signals containing two envelopes. The peaks of these envelopes correspond to the two surfaces of step structures, while the amplitude of the correct envelope corresponding to the actual bottom surface is often even lower than the other. Thus, coherence peak detection by searching the envelope with a higher amplitude is invalid and distorts the measured topography further. It is crucial to determine the correct envelope by distinguishing the current surface of step structures for each position. This can be achieved through a binarization process based on edge localization. In addition, a calculated split point dividing the anomalous coherence signals contributes to the extraction of the effective coherence signals corresponding to the correct envelope.

There have been many investigations based on interference microscopy on linewidth measurement and edge localization [13–23]. Intensity [13–16], contrast [16–18], phase [16–22], and height information pertaining to profile mutation owing to batwing effects [23], are analysed for the aforementioned purposes. Symeonidis et al. located the edges by searching the minimums in the intensity image focused on the top surface of the step structure with the height causing a π phase jump [13]. However, for a higher step height, the minimums in the intensity image are blurred owing to the weak intensity signals reflected from the bottom surface. Attota et al. studied the intensity gradients collected at different focus positions to locate the edges and subsequently measured the linewidth [14,15]. Tavrov introduced the polarization characteristics into interference microscopy and located the edges according to the minimums in the intensity and contrast map [16]. However, this method requires a relative orientation between the sample and the polarization light. Totzeck et al. adopted a similar system and interference between TE and TM components reflected from the sample was observed, while they employed the same criteria to locate the edges [17,18]. According to the above studies, analysis of the intensity and contrast information is valuable for edge localization.

In this study, we propose a method operating near the lateral resolution limit of CSI for measuring the surface topography of microstructures. The remainder of this paper is organized as follows: In Section 2, the experiment setup and characteristics of the anomalous coherence signals induced by complex diffraction effects are introduced. Section 3 describes the method for surface topography measurement of microstructures near the lateral resolution limit. Firstly, the coherence signals are pre-filtered by complete ensemble empirical mode decomposition with adaptive noise (CEEMDAN) [24]. This algorithm is an improved version of empirical mode decomposition (EMD) and has remarkable stability and efficiency for the removal of unrequired noise components from the original signals. Secondly, determination of the correct envelope is achieved by a binarization method based on edge localization. The process of edge localization integrates the contrast and intensity information. Contrast information, obtained by analysing the variation tendency of the two envelope peaks in the anomalous coherence signals, has extremums at the step edges. Intensity information is derived from the shielding effect of the microstructures and also has extremums at the step edges. Integrating these two types of information improves the accuracy of edge localization. Next, extraction of the effective coherence signals, corresponding to the correct envelope, is achieved by the Morlet wavelet transform. Finally, these effective coherence signals are calculated for surface topography measurement. Section 4 analyses the experimental results. The paper is concluded in Section 5.

2. Experiment setup and characteristics of the anomalous coherence signals

The schematic of CSI equipped with a Mirau interference microscope is shown in Fig. 1. Being different from microscopic imaging, the distinction between two points is mainly reflected in the height information for surface topography measurement. As illustrated in the right inset of Fig. 1, two sampling points are located far away from the edge of a step structure. The normal coherence signals contain a single envelope with its peak corresponding to the current surface. The topography of the step structure is recovered according to the different height information of several sampling points.

2.1. Experiment setup

To analyse the performance of CSI operating near the lateral resolution limit, the surface topography of nanopillars distributed on the metasurface is measured. Fig. 2(a) illustrates the overview schematic of the metasurface made of silicon material. Many concentric belts, represented by different colors, are distributed on the metasurface. As illustrated in Fig. 2(b), each belt contains nanopillars with space-variant geometrical parameters. The designed diameter of nanopillars ranges from 590 nm to 1350 nm, with a consistent height of 1850 nm. Period_X and Period_Y in the XY plane are 1740 nm and 3020 nm, respectively.

The coherence scanning interferometry equipment developed in our laboratory is utilized to measure the surface topography of this belt. The system is equipped with a Mirau interference objective (100 ×, NA = 0.7,

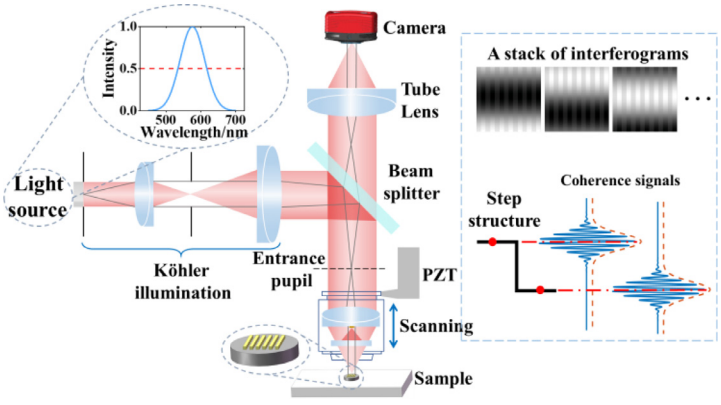

Fig. 1. Schematic of CSI.

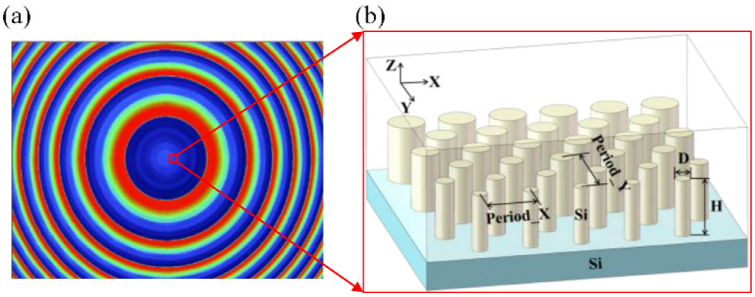

Fig. 2. Schematic of the metasurface: (a) Overview schematic; (b) Nanopillar distribution in one belt (different colour for distinguishing the substrate).

Nikon). A broadband light-emitting diode along with a light filter provides the illumination. The effective wavelength is 576 nm, considering the obliquity factor [25–27]. By controlling the scanning step as 72 nm which is equal to $\lambda_{eff}/8$ (λ_{eff} is the effective wavelength), a stack of interferograms is collected. The lateral resolution limit of the system is 501.9 nm, according to the Rayleigh criterion ($\delta_{Rayleigh} = 0.61\ \lambda/NA$, where λ is the centre wavelength of the system). Thus, when considering the features near the edges of the nanopillars and the interval between them, the measurement process is performed near the lateral resolution limit of the system. However, in this case, the anomalous coherence signals, induced by the complex diffraction effect, will mislead the coherence peak detection and further blur the characteristics of step edges in the measured topography.

2.2. Characteristics of the anomalous coherence signals

Additional fringes appear near the edges of microstructures which cause anomalous coherence signals containing two envelopes. Two cross-sectional CSI images in the XZ plane and coherence signals in different areas, as shown in Fig. 3, are sampled to exhibit these phenomena. The duty cycle is the percentage of nanopillar area in a two-dimensional period, as illustrated in the figure. Cross-Section 1 is located in an area with a high duty cycle, and the interval between nanopillars is approximately 391 nm. Cross-Section 2 is located in an area with a small duty cycle and the interval is 1138 nm. In addition, Area 1, Area 2, and Area 3 each contain eight adjacent sampling points. Fig. 4 shows the cross-sectional CSI images, and Figs. 5–7 illustrate the coherences signals in different areas.

Fig. 4 shows the dotted squares that illustrate the expected fringes, corresponding to the actual surfaces, and the additional fringes that appear even if no surfaces exist. When the interval between nanopillars approaches the lateral resolution limit of the system in Cross-Section 1, the duty cycle of the nanopillars increases and the additional fringes extend beyond the sharp edges in Fig. 4(a). Besides, compared with Fig. 4(b),

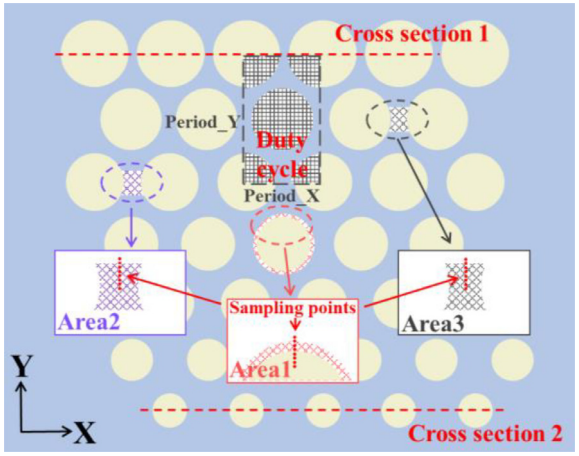

Fig. 3. Schematic of the sampling positions.

the contrast of additional fringes is even higher than expected fringes in Fig. 4(a), which induces the anomalous coherence signals containing two envelopes and distorts the coherence peak detection. The amplitude of these two envelope peaks varies regularly with the distance from the edges and the varying duty cycle. This variation tendency is defined here as the contrast information. Areas 1–3 are sampled for the analysis of the contrast information. Area 1 crosses the edges. Area 2 and Area 3 are located at the grooves, and the difference between them is the duty cycle. Each area contains eight adjacent sampling points. Figs. 5–7 show the coherence signals and the corresponding envelopes.

The scanning process of CSI is from the groove to the top of nanopillars. Thus, the right envelope corresponds to the top surface. Fig. 5(a)–(h) show the coherence signals and envelopes of the eight sampling points arranged from top to bottom in Area 1. Anomalous coherence signals appear near the edge of the nanopillar, and the amplitude of the left envelope peak is gradually lower than the right counterpart. This variation tendency is the contrast information defined above. After the sampling points cross the edges and reach the top surface of the nanopillar, as shown in Fig. 5(g) and (h), the normal coherence signals appear within twice the coherence length of the surfaces and contain a single envelope. Thus, the characteristics of contrast information facilitate locating the edges of nanopillars. However, the same phenomenon emerges in the groove areas without crossing the edges. Next, Area 2 and Area 3 are sampled to reveal this issue.

Fig. 6 shows that all the coherence signals contain two envelopes. The left envelope corresponds to the actual groove surface which has a higher amplitude than the right. The amplitude of the right envelope peak is gradually increasing, and this variation tendency is similar to that shown in Fig. 5. It seems that the greater amplitude of the right envelope peak might be a criterion for entering the top surface and the subsequent locating of the edges. However, it is not always feasible for Area 3 located in an area with a high duty cycle. In Fig. 7, the amplitude of the right envelope peak is even higher than the left one which is the same as Area 1, but Area 3 is located in the groove areas.

The amplitude of two envelope peaks for eight sampling points is extracted to illustrate the contrast information in Fig. 8. ALEP and AREP are the amplitude of the left and right envelope peaks, respectively. Fig. 8(a) shows the contrast information of eight sampling points crossing the edges and entering the top surface of nanopillars. ALEP is gradually decreasing, while AREP varies inversely. The edges can be roughly located at the intersection position of ALEP and AREP. However, for the grooves in the area with a high duty cycle, the same phenomenon arises, as shown in Fig. 8(c). By contrast, in the groove area with a small duty cycle, ALEP is always higher than AREP in Fig. 8(b). To summarise, the contrast information is not sufficient for locating the edges. It is necessary to distinguish the contrast information between the areas as Area 1 and Area 3.

2.3. Construction of the coherence functions, considering the complex diffraction effect

In terms of studying the anomalous coherence signals, rigorous coupled-wave analysis (RCWA) is employed for modelling the coherence functions [11]. The low-coherence light source with Gaussian spectral

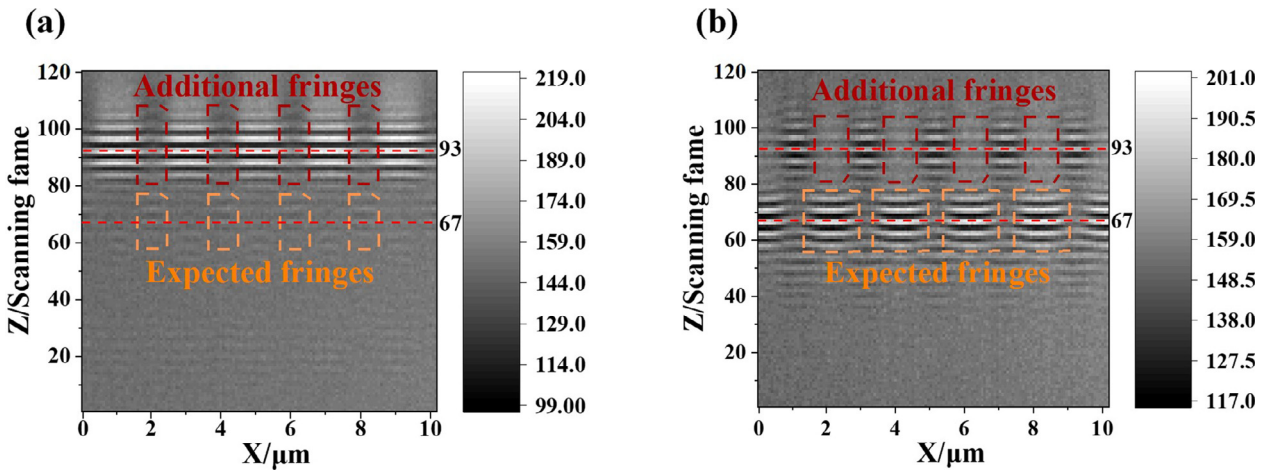

Fig. 4. Cross-sectional CSI images in the XZ plane. (a) Cross-Section 1. (b) Cross-Section 2.

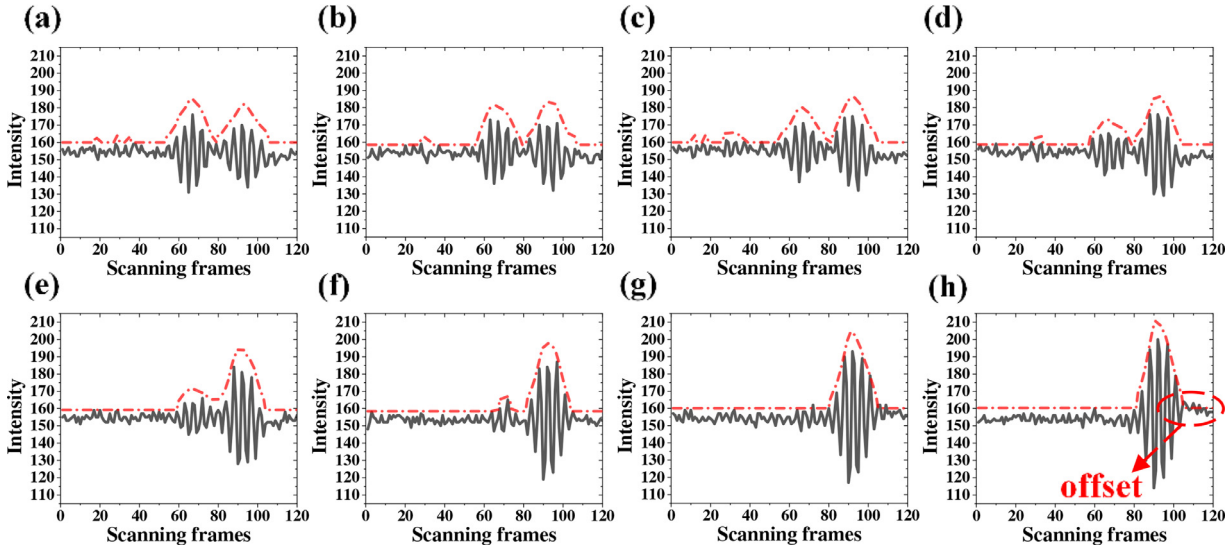

Fig. 5. Coherence signals (black solid line) and the corresponding envelopes (red dashed line) in Area 1 marked in Fig. 3.

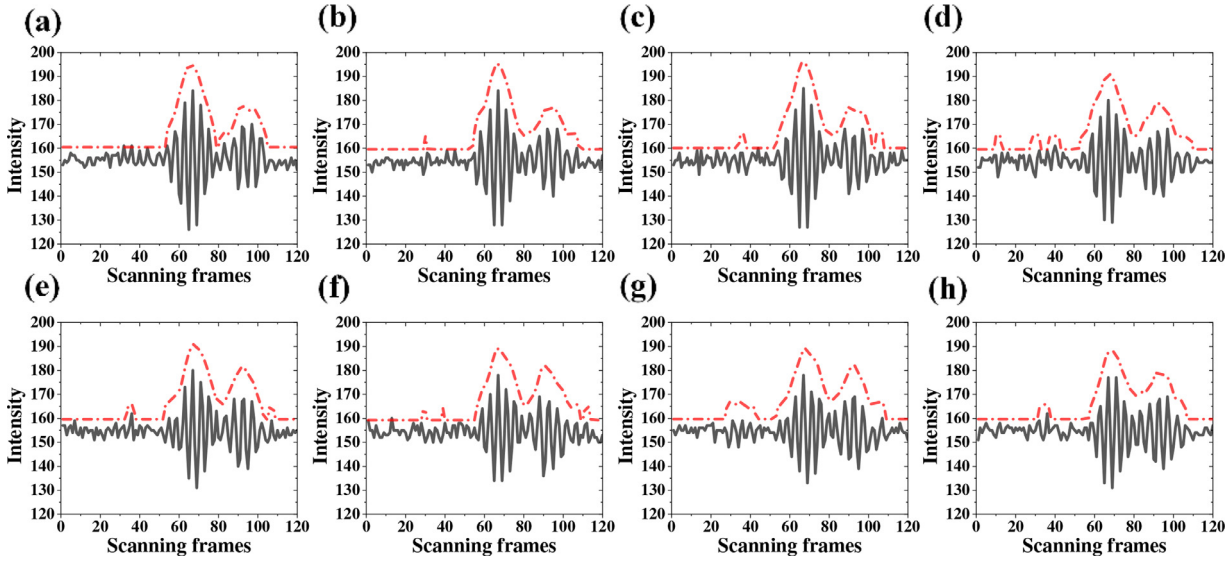

Fig. 6. Coherence signals (black solid line) and the corresponding envelopes (red dashed line) in Area 2 marked in Fig. 3.

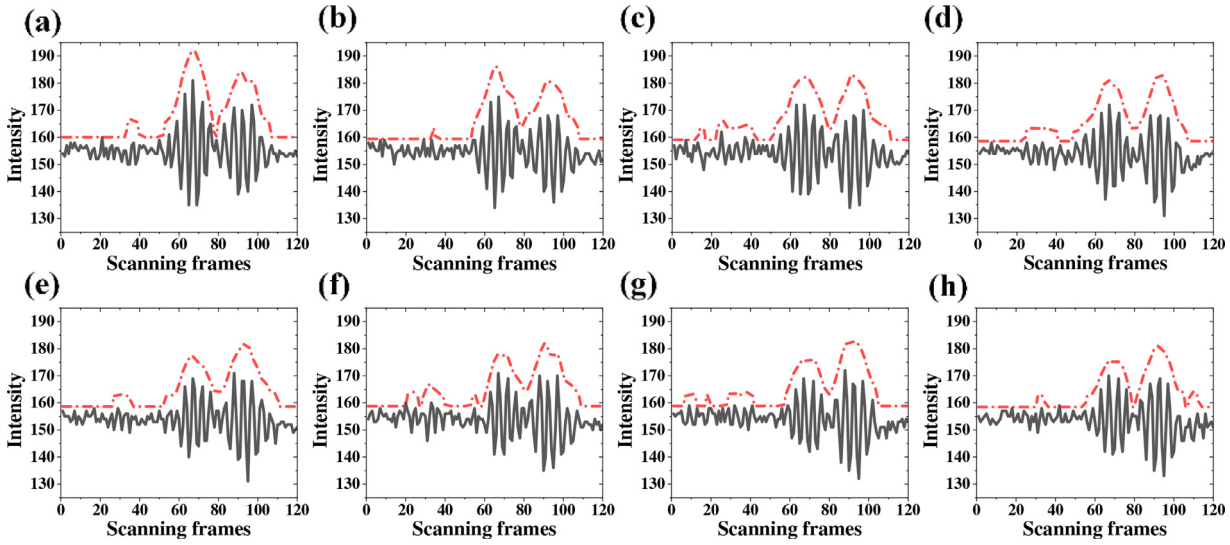

Fig. 7. Coherence signals (black solid line) and the corresponding envelopes (red dashed line) in Area 3 marked in Fig. 3.

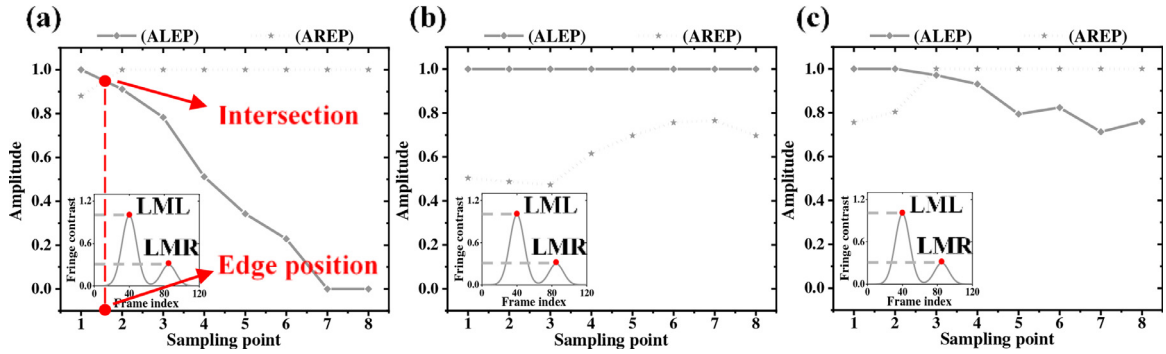

Fig. 8. Contrast information: ALEP represents the amplitude of the left envelop peak; AREP represents the amplitude of the right envelop peak. (a)–(c) correspond to Areas 1–3 marked in Fig. 3. The amplitude has been normalized.

distribution illuminates the entrance pupil, adopting the formation of Köhler illumination. It is equivalent to multiple plane waves with different spatial frequencies illuminating the measured sample. The application of RCWA establishes the light field of the incident light interacting with the sample [28,29]. The reflection light passes through the objective lens and converts to the spatial-frequency spectrum at the exit pupil. According to the coherent transfer function, the Jones vector is expressed as follows:

$$J_{x,y,z} = \sum_{w} S(w) \times \sum_{\mu} L(\mu) \times \left\{ \sum_{v} \exp(ik_v \cdot r) \cdot cos^{\frac{1}{2}}(v) \cdot \mathcal{F}^{-1}\left(H(v) \cdot \begin{bmatrix} \mathcal{F}\{E_x(k_{\mu,w})\} \\ \mathcal{F}\{E_y(k_{\mu,w})\} \end{bmatrix} \right) \right\}^2, \quad (1)$$

where the subscript w denotes the wavelength of light source, μ denotes the illumination angle, v varies from 0 to θ_{max}, where θ_{max} is related to the numerical aperture of the objective by $NA = n \cdot sin(\theta_{max})$. $S(w)$ is the spectral intensity. $L(\mu)$ is the intensity distribution corresponding to the illumination angle. $H(v)$ is the coherence transfer function of the objective. In Eq. (1), $cos^{1/2}(v)=(k_0^2-k_x^2-k_y^2)^{1/2}/k_0$. E is the light field distribution on the sample surface according to RCWA and comprises two orthogonal polarization components.

The coherence signals are given by

$$I = (J_1 + J_2)^T (J_1 + J_2)^*, \quad (2)$$

where the superscript T denotes transpose operation of the matrix, and * represents the complex conjugation. For the object beam, J_1 is equal to $J_{x,y,z}$ demonstrated in Eq. (1). J_2 represents the reference beam whose polarization state is the same as the incident light. Moreover, the scanning procedure is added into the object arm and Eq. (1).

3. Surface topography measurement of nanopillars near the lateral resolution limit

We propose a method including four main steps for the measurement of the surface topography of microstructures near the lateral resolution limit. Firstly, coherence signals are pre-filtered by CEEMDAN for eliminating the local offset and the noise components. Secondly, the correct envelope is determined by a binarization method based on edge localization. The contrast and intensity information are integrated by constructing orthometric searching paths to locate the edges. Next, the Morlet wavelet transform with a new construction form of the wavelet family is performed to calculate a split point dividing the anomalous coherence signals, and the effective coherence signals corresponding to the correct envelope are extracted. Finally, with the integration of the coherence and phase information calculated by the effective coherence signals, the surface topography of nanopillars is recovered. The detailed process is illustrated in Fig. 9.

3.1. Process of pre-filtering

As shown in Figs. 5–7, the noise components in the coherence signals corresponding to the groove areas are evident. In addition, in Fig. 5(h), the local offset appears in the coherence signals. Therefore, pre-filtering

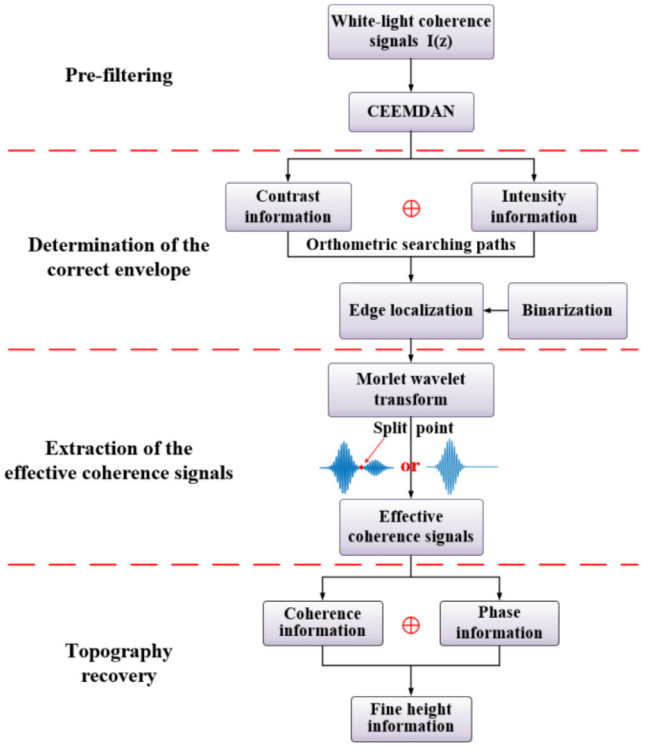

Fig. 9. Flow chart of the proposed method.

is essential for removing these components and improving the signal-to-raise ratio of original coherence signals. CEEMDAN is an improved version of EMD and can effectively remove the useless components in the original signals. This algorithm has been employed for suppressing the batwing effect and the results have been verified based on the experiment results reported in Ref. [30]. The coherence signals are decomposed into oscillatory components called intrinsic mode functions (IMFs). Replacing the original signals with the selected IMF can filter out the unrequired components, and the criterion function is as follows:

$$S = \sqrt{\frac{1}{n}\sum_{i=1}^{n}\left[I_k(i) - I(i)\right]^2}, \tag{3}$$

where I_k is the different IMFs, I is the original signals, and n represents the total scanning frames.

The IMF whose S attains the minimum value, is considered as the substitute of the original signals. As illustrated in Fig. 10(a), the original signals are decomposed into eight IMFs. According to Eq. (3), IMF1 is selected without attenuating the contrast of the original signals, while the local offset is removed compared with the original signals in Fig. 10(b). Next, IMF1 is processed for subsequent calculation.

3.2. Determination of the correct envelope by binarization based on edge localization

Weak intensity signals contribute to edge localization because the nanopillars shield the reflected light from the bottom edge. The maximum of the coherence signals is extracted and is given by

$$I_{select}(x, y) = \max(I(x, y, z)), \tag{4}$$

where $I(x,y,z)$ denotes the coherence signals of each pixel. As shown in Fig. 11(a), a new intensity map is stitched by $I_{select}(x,y)$ of all pixels, wherein the nanopillars are surrounded with weak intensity signals.

The red sampling line is drawn in Fig. 11(a) for utilizing the intensity information given by

$$I_{inf}(i) = \frac{I_{selsct}(i)}{\max\left(I_{selsct}(1)\cdots I_{selsct}(i)\cdots I_{selsct}(N)\right)} - 1, \tag{5}$$

where $I_{inf}(i)$ represents the intensity information of the ith point on the sampling line, N is the total number of sampling points on the line, and $I_{select}(i)$ is defined in Eq. (4). Due to the shielding of the nanopillars, $I_{inf}(i)$ obtains the minimums at the edges.

However, in the golden rectangle of Fig. 11(a), the edges are blurred in the groove areas with a high duty cycle. According to the analysis in Section 2.2, the contrast information can be utilized for edge localization, but it is also invalid in the same groove areas. The combination of intensity and contrast information is a method of locating the edges precisely. As illustrated in the inset of Fig. 11(a), the current point marked in black is sampled amongst ten adjacent points. The contrast information of the current point is calculated as follows:

$$C_{inf}(i) = \left[\sum_{i-1}^{i-N} ALEP(i) - \sum_{i+1}^{i+N} ALEP(i)\right] + \left[\sum_{i+1}^{i+N} AREP(i) - \sum_{i-1}^{i-N} AREP(i)\right], \tag{6}$$

where i represents the current point, and *ALEP* and *AREP* are the amplitude of the left and right envelope peaks, respectively. N is the sampling length which is set as 5 in the experiment. According to the contrast information, $C_{inf}(i)$ also exhibits extremums at the edges. Either *ALEP* or *AREP* is set to zero for the normal coherence signals. Determination of the anomalous coherence signals and extraction of ALEP (or AREP) are introduced in Section 3.3.

Finally, the contrast and intensity information are integrated by multiplying the corresponding points between $C_{inf}(i)$ and $I_{inf}(i)$ to highlight the extremums at the edge. The result of the red sampling line (vertical searching path) is shown in Fig. 11(b). Several maximums and minimums appear in pairs entering and leaving the top surface, respectively. However, the anomalous maximum is observed. This position is located within the golden rectangle in Fig. 11(a) where the duty cycle is high. Therefore, the maximum and minimum values are selected in pairs.

According to the vertical searching paths, binarization is achieved based on edge localization, as shown in Fig. 12(a). However, the minimum interval that can be resolved is 387 nm, corresponding to six sampling pixels based on this method. Therefore, it is invalid to distinguish the critical dimension of the nanopillars and the same conditions also appear in transverse searching paths, as shown Fig. 12(b). To solve this issue, the results of these two searching paths are superimposed. As shown in Fig. 12(c), even if the interval between nanopillars and their chord length is near the lateral resolution limit of the system (501.9 nm, according to the Rayleigh criterion), they are distinguished precisely.

The binarization process identifies the current surface for each position, while the correct envelope corresponding to this surface is determined in the anomalous coherence signals.

3.3. Extraction of the effective coherence signals corresponding to the correct envelope

When located far away from the step edges of nanopillars, the normal coherence signals contain a single envelope. For the position near the edges, the anomalous coherence signals contain two envelopes. The following process is implemented to identify the anomalous coherence signals and calculate a split point dividing these signals. Next, the effective coherence signals corresponding to the correct envelope are extracted.

We propose a novel construction method of wavelet family in the Morlet wavelet transform to achieve this purpose. The mother wavelet function is obtained by

$$\varphi(z) = e^{(-z^2/2)}e^{i\omega_0 z}, \tag{7}$$

where w_0 denotes the centre frequency. By controlling the scaling factor a, and the shifting factor b, the wavelet family (z,a,b) is constructed

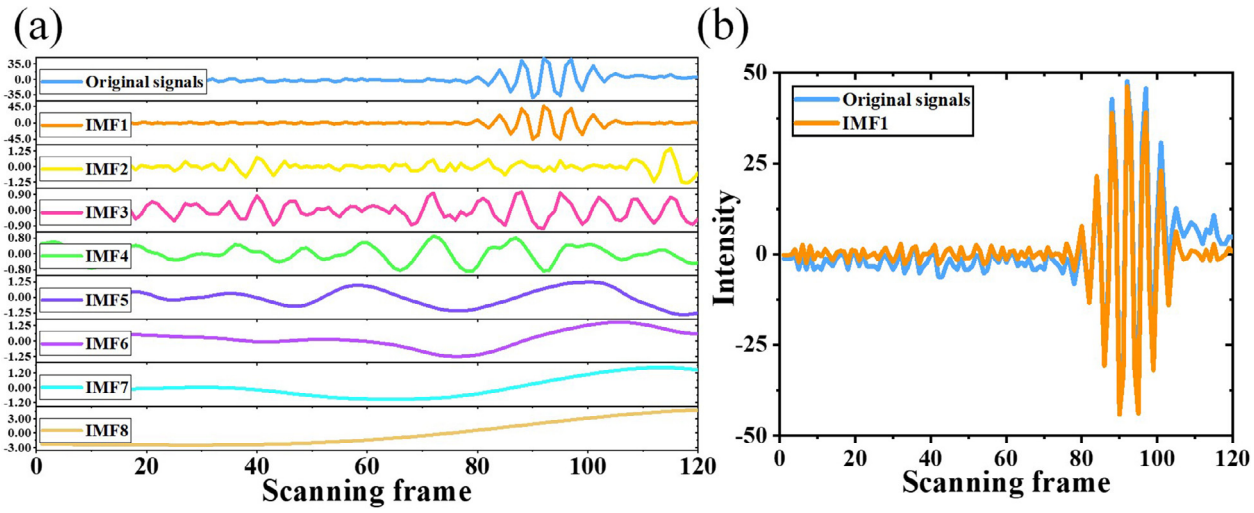

Fig. 10. Results of pre-filtering: (a) Decomposition results of CEEMDAN; (b) Selected IMF.

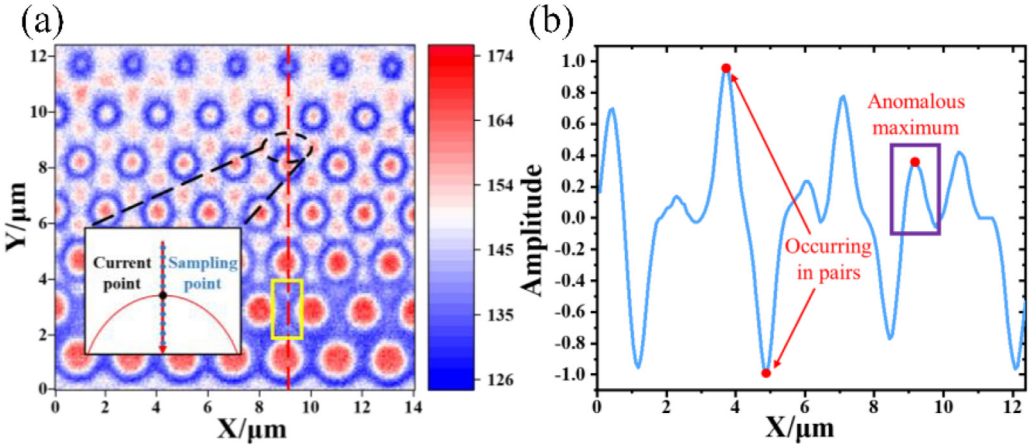

Fig. 11. (a) Stitching intensity map; (b) Result of vertical searching path (normalized to lie within ±1).

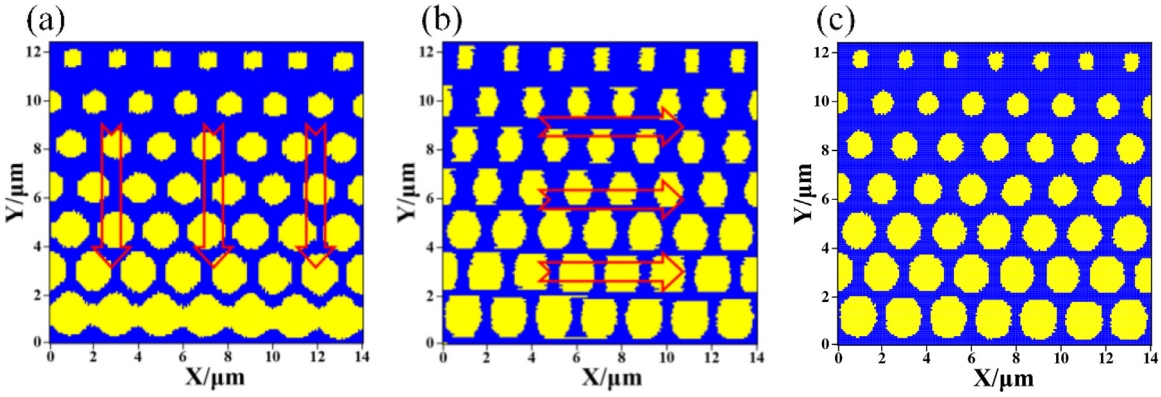

Fig. 12. Binarization based on edge localization: (a), (b) Vertical and transverse searching paths; (c) Superimposed result.

according to Eq. (8).

$$\varphi(z,a,b)=\frac{1}{\sqrt{a}}\left[\varphi\left(\frac{z-b}{a}\right)+\varphi\left(\frac{z+b}{a}\right)\right] \tag{8}$$

As shown in Fig. 13(a), the pink signal is the constructed wavelet function containing two branches. By changing the shifting factor b, the interval between these two branches varies. The constructed wavelet function slides along the coherence signals through convolution. The proposed wavelet transform function of the coherence signals $I(z)$ is expressed as

$$WT(z,b)=\int_{-\infty}^{+\infty} I(z)dz\int_{int_1}^{int_2}\varphi^*(z,a,b)db, \tag{9}$$

where $\varphi^*(z,a,b)$ denotes the conjugate of $\varphi(z,a,b)$, and int_1 and int_2 are the intervals between the two branches. The scaling factor a is set to be a constant.

The wavelet coefficient of the coherence signal is derived from

$$|WT(z,b)|=\sqrt{\left(WT_r(z,b)\right)^2+\left(WT_i(z,b)\right)^2}, \tag{10}$$

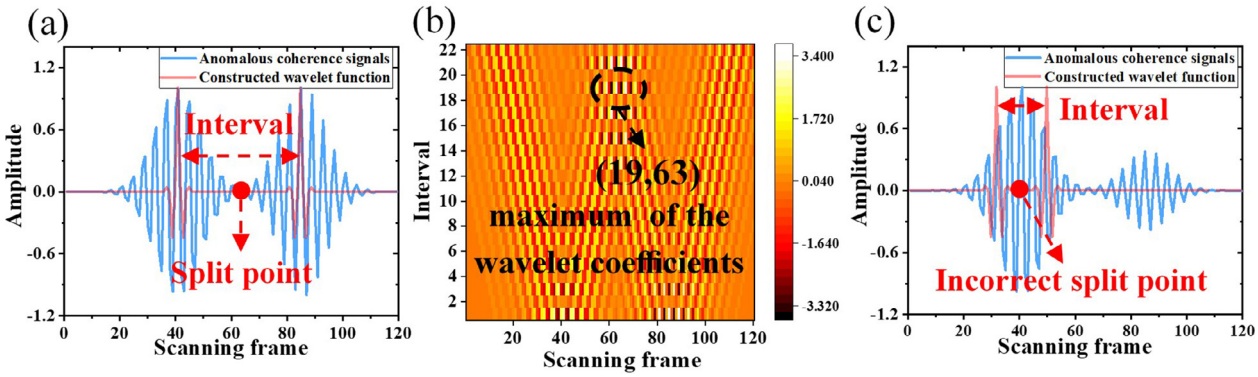

Fig. 13. Results of the wavelet transform: (a) Correct split point; (b) Wavelet coefficients; (c) Incorrect split point owing to small int_1.

where $WT_r(z,b)$ and $WT_i(z,b)$ are the real part and imaginary part of $WT(z,b)$, respectively.

Fig. 13(b) shows the coordinates when the wavelet coefficient attains its maximum. The current sliding position (named as 63 in the figure) is determined as the split point that divides the anomalous coherence signals into two parts. If int_1 is set to an extremely small value, the constructed wavelet function falls into one part of the signals and induces an incorrect split point, as shown in Fig. 13(c). In the experiment, the suitable int_1 and int_2 are set to be 5 and 25, respectively. For the normal coherence signals, the maximal wavelet coefficient is lower than the anomalous coherence signals, owing to the lower correlation between the input signals and wavelet functions. Hence, the proposed method can identify the anomalous coherence signals and divide these signals automatically.

3.4. Surface topography measurement of nanopillars

According to the above process, the normal and effective coherence signals are determined for surface topography measurement. We implement Morlet wavelet transform to extract the envelope, and the cubic spline interpolation to complete the results. Envelope peak positions of all the pixels compose the coherence information which is further combined with added phase information to improve the axial measurement accuracy. As mentioned in Section 2.1, the phase information is calculated using the effective wavelength concerning the obliquity factor:

$$z_{phase} = \frac{\varphi}{2 \cdot k}, \tag{11}$$

where $k = 2\pi/\lambda_{eff}$, λ_{eff} is the effective wavelength, and φ corresponds to the phase of all the pixels.

These two types of information are integrated by the algorithm, high-definition vertical scanning interferometry (HDVSI) [31].

4. Experimental results

To confirm the validity and feasibility of the proposed method, the surface topography of seven types of nanopillars on the metasurface is measured, and the result is shown in Fig. 14(a) and Table 1. The diameter and the height of different nanopillars are detected via scanning electron microscopy (SEM) for comparison.

Table 1
Measurement results of the proposed method.

Nanopillar type	Diameter PM (nm)	Diameter SEM (nm)	Height PM (nm)	Duty cycle
1	595.8 ± 24.6	602.1 ± 20.2	1842.3 ± 29.2	0.24
2	808.7 ± 56.8	788.9 ± 34.9	1855.5 ± 14.9	0.18
3	1003.8 ± 40.9	897.0 ± 18.0	1849.3 ± 18.7	0.24
4	1108.1 ± 29.2	974.0 ± 28.4	1840.4 ± 16.8	0.29
5	1295.1 ± 36.6	1095.8 ± 29.4	1822.2 ± 19.6	0.36
6	1365.9 ± 34.9	1189.9 ± 28.3	1818.1 ± 20.7	0.44
7	1440.0 ± 34.7	1348.6 ± 12.4	1831.4 ± 30.3	0.40

Two adjacent interferograms in the focal depth range of the top surface are shown in Fig. 15(a, b), wherein the images of nanopillars are blurred compared with the SEM images. The critical dimension of nanopillars and the interval between them are near the lateral resolution limit. In this case, the anomalous coherence signals impact the coherence peak detection, as mentioned in Section 2.2. Thus, it is significant to improve the accuracy of topography measurement for microstructures near the lateral resolution limit. In Fig. 14(a), the topography of seven types of nanopillars is successfully recovered by the method proposed in this paper.

In Table 1, the duty cycle, mentioned in Section 2.2, indicates the space density for the current type of nanopillars:

$$Duty\ cycle = A_{nanopillars}/(Period\_X \times Period\_Y), \tag{12}$$

where $Period\_X$ and $Period\_Y$ are periods in two directions, $A_{nanopillars}$ is the total area centred on the current type of nanopillars, illustrated in Fig. 3. It is worth noting that these seven types of nanopillars belong to one belt located between the same two belts. Thus, the duty cycles of nanopillars in Row 1 and Row 7 are slightly different.

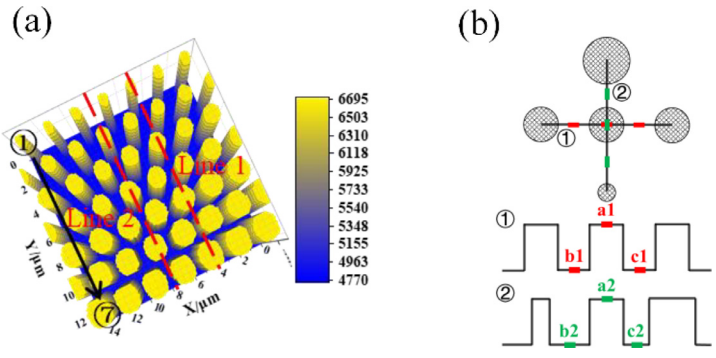

Fig. 14. (a) Measurement results of the proposed method. (b) Schematic of the height assessment.

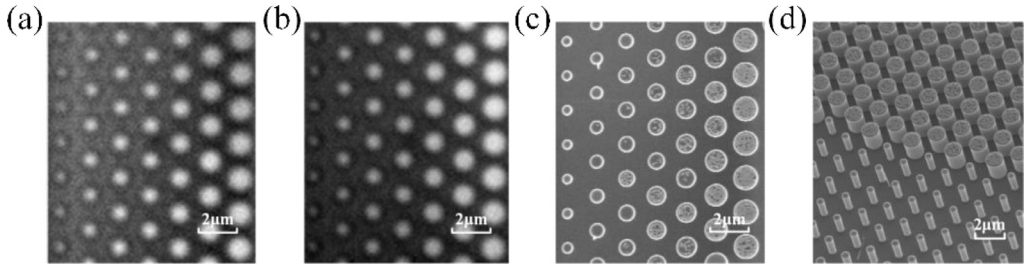

Fig. 15. (a, b) Two adjacent scanning interferograms in the focal depth range of the top surface. (c, d) SEM images.

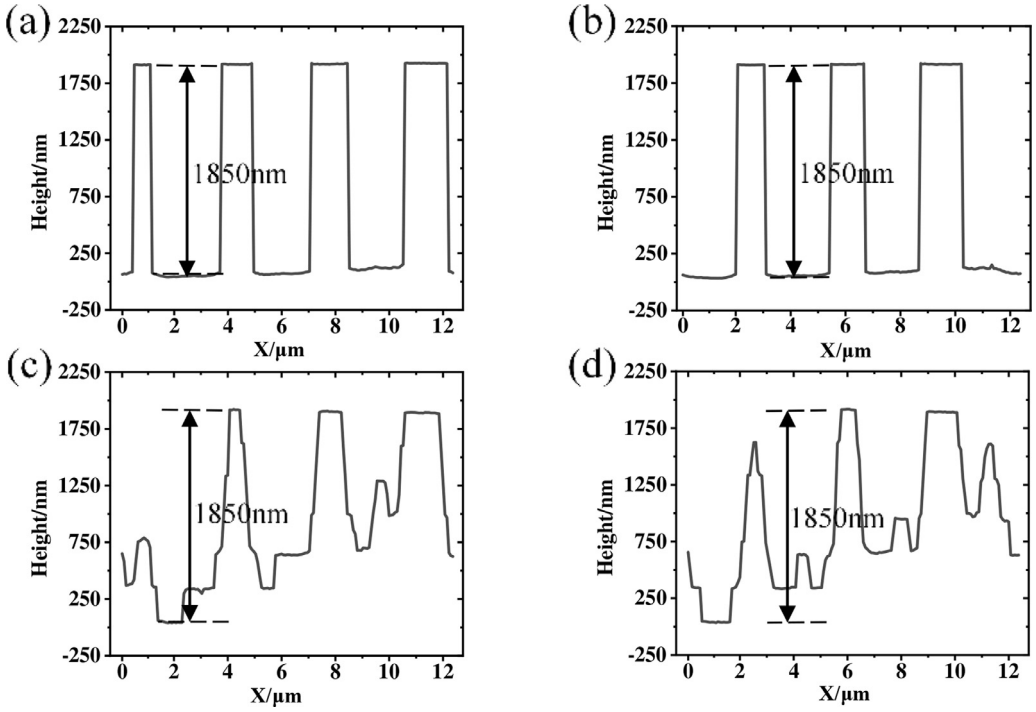

Fig. 16. Cross-sectional profile of Line 1 and Line 2 marked in Fig. 14(a): (a), (b) Profile calculated by the proposed method; (c), (d) Profile calculated by the original coherence signals using HDVSI.

As analysed in Section 2.2, the characteristics of the coherence signals vary with the distance from the edges. Different from the assessment of the step height from a single sampling line, the height of one type of nanopillars is calculated from two crossing sampling lines. The sampled positions are marked in Fig. 14(b), and the height is calculated using

$$H = [(a1 - b1) + (a1 - c1) + (a2 - b2) + (a2 - c2)]/4. \quad (13)$$

The fidelity of the recovery topography is evaluated from the measured diameter and height of the nanopillars. The mean value and standard deviation for a certain type of nanopillar, are calculated based on all the nanopillars of the same type in the measured area. In Table 1, the diameters calculated by the proposed method (Diameter PM) are slightly larger than the SEM results (Diameter SEM) for the nanopillars in rows 2–7. It is the large duty cycle that causes the narrow space between the nanopillars. For instance, the smallest interval between two nanopillars is only 391 nm in row 7. In this case, the energy of reflected light is exceedingly weak for ensuring a high signal-to-noise ratio of the coherence signals. This impacts the edge localization and induces a larger measured diameter. However, the deviations between Diameter PM and Diameter SEM are within 200 nm, and the standard deviation of the proposed method is near the SEM result.

Fig. 16 illustrates the measured cross-sectional profiles of two sampled lines passing through different nanopillars (marked in Fig. 14(a)). As introduced in Section 3.4, the normal and effective coherence signals are determined for profile measurement. Comparison is performed with the profile calculated by HDVSI using the original coherence signals. Due to the existence of anomalous coherence signals, the measured profile of the nanopillars is distorted compared with the proposed method. The height of different types of nanopillars is assessed using Eq. (13) and defined as Height PM in Table 1. The deviations between Height PM and SEM results (1850 nm) are within 31.9 nm, and the standard deviations of Height PM are smaller than 30.3 nm which verifies the accuracy and the repeatability of the proposed method. Given the critical dimensions of the nanopillars, topography measurement is realized near the lateral resolution limit.

5. Conclusions

In this paper, we propose a method for measuring the surface topography of microstructures near the lateral resolution limit of CSI. The prefiltering process eliminates the offset and noise components in the coherence signals by CEEMDAN. Next, the contrast and intensity information are integrated by the constructed orthometric searching paths for locating the edges. Binarization based on edge localization distinguishes the current surface of each position and determines the correct envelope in the anomalous coherence signals. Morlet wavelet transform with a new construction of the wavelet family provides a split point, dividing the anomalous coherence signals, and the effective coherence signals corre-

sponding to the correct envelope are extracted for topography measurement. The consistency of the measurement results between the proposed method and SEM is confirmed, and a height deviation within 31.9 nm is observed. In addition, the standard deviation of the detected diameter and height by the proposed method is less than 56.8 nm and 30.3 nm, respectively. Experimental results demonstrate the accuracy and the stability of the proposed method employed for topography measurement of space-variant samples. Due to the general trend towards miniaturization, this non-destructive metrology offers significant advantages in surface topography measurement near the lateral resolution limit, without introducing any physical upgrade to the instrument.

Disclosures

The authors declare no conflicts of interest.

Declaration of Competing Interest

None.

Acknowledgements

This work was supported by the National Key Research and Development Program [Grant No. 2019YFB2005500]; National Natural Science Foundation of China [Grant Nos. 62175107, U1931120]; Six talent peaks project in Jiangsu Province [Grant No. RJFW-019]; Foundation of key laboratory of optical system advanced manufacturing technology, Chinese academy of sciences [Grant No. KLOMT190201]; Foundation of Shanghai key laboratory of online test and control technology [Grant No. A04202130002].

References

[1] Bruzzone AAG, Costa HL, Lonardo PM, Lucca DA. Advances in engineered surfaces for functional performance. CIRP Ann 2008;57:750–69.
[2] Coupland J, Mandal R, Palodhi K, Leach R. Coherence scanning interferometry: linear theory of surface measurement. Appl Opt 2013;52:3662–70.
[3] Su R, Thomas M, Liu M, Drs J, Bellouard Y, Pruss C, Coupland J, Leach R. Lens aberration compensation in interference microscopy. Opt Lasers Eng 2020;128:106015.
[4] Su R, Thomas M, Leach R, Coupland J. Effects of defocus on the transfer function of coherence scanning interferometry. Opt Lett 2018;43:82–5.
[5] Su R, Wang Y, Coupland J, Leach R. On tilt and curvature dependent errors and the calibration of coherence scanning interferometry. Opt Express 2017;25:3297–310.
[6] Lehmann P, Xie W, Allendorf B, Tereschenko S. Coherence scanning and phase imaging optical interference microscopy at the lateral resolution limit. Opt Express 2018;26:7376–89.
[7] Xie W, Lehmann P, Niehues J, Tereschenko S. Signal modeling in low coherence interference microscopy on example of rectangular grating. Opt Express 2016;24:14283–300.
[8] Lehmann P, Xie W, Niehues J. Transfer characteristics of rectangular phase gratings in interference microscopy. Opt Lett 2012;37:758–60.
[9] Thomas M, Su R, Nikolaev N, Coupland J, Leach R. Modeling of interference microscopy beyond the linear regime. Opt. Eng. 2020;59:034110.
[10] Coupland J, Lobera J. Measurement of steep surfaces using white light interferometry. Strain 2010;46:69–78.
[11] Tavrov A, Schmit J, Kerwien N, Osten W, Tiziani H. Diffraction-induced coherence levels. Appl Opt 2005;44:2202–12.
[12] Sun Y, Yu H, Ma J, Hu Q, Huang X, Zhou J, Xie P, Yang Z, Lei L, Fu Y, Gao Z, Yuan Q. Additional fringe processing for dielectric metasurface profile measurement using white-light scanning interferometry. Appl Opt 2021;60:215–23.
[13] Symeonidis M, Nakagawa W, Kim DC, Hermerschmidt A, Scharf T. High-resolution interference microscopy of binary phase diffractive optical elements. OSA Contin 2019;2:2496–510.
[14] Attota R, Germer TA, Silver RM. Through-focus scanning-optical-microscope imaging method for nanoscale dimensional analysis. Opt Lett 2008;33:1990–2.
[15] Attota R, Silver R, Dixson R. Linewidth measurement technique using through-focus optical images. Appl Opt 2008;47:495–503.
[16] Tavrov A. Rigorous coupled-wave analysis calculus of submicrometer interference pattern and resolving edge position versus signal-to-noise ratio. Opt Eng 2002;41:1886–92.
[17] Totzeck M, Jacobsen H, Tiziani HJ. Edge localization of subwavelength structures by use of polarization interferometry and extreme-value criteria. Appl Opt 2000;39:6295–305.
[18] Totzeck M, Tiziani HJ. Phase-shifting polarization interferometry for microstructure linewidth measurements. Opt Lett 1999;24:294–6.
[19] Hai HH, Chen LC, Nguyen DT, Lin ST, Yeh SL, Yao Y. Accurate submicron edge detection using the phase change of a nano-scale shifting laser spot. Opt Laser Technol 2017;92:109–19.
[20] Creath K. Submicron linewidth measurement using an interferometric optical profiler. In: Integrated circuit metrology, inspection, and process control v, 1464. International Society for Optics and Photonics; 1991. p. 474–83.
[21] Zhou W, Cai L. Method for edge detection based on phase jump in a differential interferometer. Appl Opt 1999;38:152–9.
[22] Zhou W, Cai L. Edge location by use of optical phase variation. Appl Opt 2000;39:2569–76.
[23] Topfer SC, Kuhn O, Linss G. Model-based edge detection in height map images with nanometer resolution. In: Photonics north 2004: photonic applications in astronomy, biomedicine, imaging, materials processing, and education, 5578. International Society for Optics and Photonics; 2004. p. 476–85.
[24] Torres ME, Colominas MA, Schlotthauer G, Flandrin P. A complete ensemble empirical mode decomposition with adaptive noise. In: Proceedings of the IEEE international conference on acoustics, speech and signal processing (ICASSP). IEEE; 2011. p. 4144–7.
[25] Sheppard CJR, Larkin KG. Effect of numerical aperture on interference fringe spacing. App. Opt 1995;34:4731–4.
[26] Creath K. Calibration of numerical aperture effects in interferometric microscope objectives. Appl. Opt 1989;28:3333–8.
[27] Dubois A, Selb J, Vabre L, Boccara AC. Phase measurements with wide-aperture interferometers. Appl Opt 2000;39:2326–31.
[28] Moharam MG, Grann EB, Pommet DA, Gaylord TK. Formulation for stable and efficient implementation of the rigorous coupled-wave analysis of binary gratings. J Opt Soc Am A 1995;12:1068–76.
[29] Moharam MG, Pommet DA, Grann EB, Gaylord TK. Stable implementation of the rigorous coupled-wave analysis for surface-relief gratings: enhanced transmittance matrix approach. J Opt Soc Am A 1995;12:1077–86.
[30] Sang M, Du X, Wang S, Xu T, Dong J, Liu T. Gap-matching algorithm with the impCEEMDAN in scanning white-light interference microscopy. Opt Express 2020;28:15101–11.
[31] Chen D, Schmit J, Novak M. In: Real-time scanner error correction in white light interferometry, 9276; 2014. p. 92760I.